ANGSTROM TO MILLIMETER CHARACTERIZATION OF ROCK PORE STRUCTURE AND THE PREDICTION OF CONDUCTIVITY AND PERMEABILITY THEREOF

E.S. Amirtharaj and M.A. Ioannidis
Department of Chemical Engineering, University of Waterloo

This paper was prepared for presentation at the International Symposium of the Society of Core Analysts held in Abu Dhabi, UAE, 5-9 October 2004

ABSTRACT

A method for determining the continuous distribution of pore sizes within a porous solid over the range 0.01-1000 □m (Amirtharaj *et al*., 2003) is applied to a suite of sandstone and carbonate rocks and the usefulness of the results obtained is evaluated with respect to the prediction of formation factor and permeability. The method employs a statistical description of the microstructure to combine information from mercury intrusion porosimetry (MIP) and binary micrographs of the pore space. Direct comparison of the distribution of pore volume by pore size to the distribution of pore volume by access pore *throat* size (MIP data) enables the estimation of an apparent pore-to-throat aspect ratio for each pore size. Using a model of constricted circular tubes to represent individual pore channels, critical path analysis (CPA) is employed to derive predictive equations for the formation factor and permeability. The new equations predict the permeability and formation factor of the test samples, both to within a factor of 1.7 (± 0.7). We find that accounting for both pore and throat sizes leads to significant improvement in the prediction of formation factor over what is possible using previous results. Finally, we suggest that estimates of the apparent pore-to-throat aspect ratio may be used to predict the residual non-wetting phase saturation during quasistatic secondary imbibition under strongly water-wet conditions and estimate initial-residual non-wetting phase saturation relations for different porous rocks.

INTRODUCTION

A new method of pore structure characterization based on the statistical fusion of small-angle neutron scattering (SANS) and backscatter SEM imaging data and their subsequent interpretation in terms of a polydispersed spherical pore (PDSP) model was recently proposed (Radlinski *et al*., 2004). Application of this method to a sample of reservoir sandstone provided the pore size distribution in the range 1 nm to 1 mm, probing both fractal and Euclidean aspects of the microstructure. The pore size information thus obtained was shown to be consistent with and complementary to MIP and NMR relaxation data. A modification of this method was also proposed (Amirtharaj *et al*, 2003), whereby information normally provided by SANS measurements is substituted

approximately by a fractal scaling law using estimates of the surface fractal dimension obtained by MIP (Ehrburger-Dolle *et al*., 1994):

$$-dS_{Hg}/dr \propto r^{2-D}, \tag{1}$$

where $S_{Hg}(r)$ is the sample saturation to mercury at capillary pressure $P_c \propto 1/r$. The method assumes that the pore space can be represented by an assembly of independent spherical pores with an arbitrary distribution $f(R)$ of radii R, in which case the cumulative distribution of pore volume by pore size is given by:

$$F(R) = \langle V_R \rangle^{-1} \int_R^{R_{\max}} V_r f(R) dR. \tag{2}$$

where $R_{\max}$ and $R_{\min}$ are the maximum and minimum pore radii, respectively, $V_R \equiv V(R) = (4/3)\pi R^3$ is the volume of a sphere of radius R and $\langle V_R \rangle = \int_{R_{\min}}^{R_{\max}} V_r f(R) dR$ is the average pore volume. If the pore space were an assembly of disconnected pores (spheres or cylinders with length equal to their diameter), then we should expect $r = R$ for $S_{Hg}(r) = F(R)$, *i.e*., the two functions should be identical. In reality, the pore space is interconnected. Large pores may be surrounded by smaller ones and each pore is accessible through constrictions in its immediate vicinity (pore throats), both situations causing pores of size R to be invaded by mercury at a capillary pressure higher than the one corresponding to their size. As a result, $S_{Hg}(r) = F(R)$ for $r < R$ and the ratio $\lambda = R/r$ for which $S_{Hg}(r) = F(R)$ corresponds to an *apparent* pore-to-throat size aspect ratio for pores of size R. This is novel information that may be related to the magnitude of water-flood residual oil saturation and can be used to improve models of permeability and electrical conductivity based on critical path analysis (CPA), as explained next.

PERMEABILITY AND CONDUCTIVITY FROM CPA

Assuming that individual pore space channels are cylinders of length equal to their diameter ℓ, Katz and Thompson (1987) obtained the following expressions for the permeability and conductivity from CPA:

$$k_{KT} = (1/89)(\ell^h_{\max}/\ell_c)\phi(\ell^h_{\max})^2\left(S_{Hg}(\ell^h_{\max}) - S_{Hg,c}\right), \tag{3}$$

$$F_{KT}^{-1} = (\ell^e_{\max}/\ell_c)\phi\left(S_{Hg}(\ell^e_{\max}) - S_{Hg,c}\right), \tag{4}$$

Here, the threshold saturation $S_{Hg,c} \equiv S_{Hg}(\ell_c)$ corresponds to the point at which the mercury first forms a sample-spanning cluster and is identified with the inflection point of the mercury intrusion curve, whereas $\ell^h_{\max}$ and $\ell^e_{\max}$ are characteristic length scales for permeability and conductivity, respectively, determined by maximizing $g_h \propto \ell^3\left[S_{Hg}(\ell) - S_{Hg,c}\right]$ and $g_e \propto \ell\left[S_{Hg}(\ell) - S_{Hg,c}\right]$. Consistent with the new pore structure information provided in this work, we idealize individual pore space channels as

constricted cylinders (see Fig. 1). Accordingly, the trial functions for permeability and conductivity, g_h and g_e, are written as:

$$g_h \propto R^3\left(F(R) - S_{Hg,c}\right) \Bigg/ \left[\frac{16(1+\lambda^3)}{\pi} + \frac{3\lambda(\lambda^2-1)}{2}\right], \tag{5}$$

$$g_e \propto \frac{R}{(1+\lambda)}\left(F(R) - S_{Hg,c}\right), \tag{6}$$

where the apparent aspect ratio λ is a function of pore size *R*. For this model, critical path analysis leads to the following expressions for the permeability and formation factor:

$$k = \frac{2\phi(\lambda^h_{\max}+1)(R^h_{\max})^2}{\pi\lambda^h_{\max}\left\{\frac{16[1+(\lambda^h_{\max})^3]}{\pi} + \frac{3\lambda^h_{\max}[(\lambda^h_{\max})^2-1]}{2}\right\}}\left(F(R^h_{\max}) - S_{Hg,c}\right), \tag{7}$$

$$F = \left(\frac{\lambda^e_{\max}}{\phi}\right)\left(F(R^e_{\max}) - S_{Hg,c}\right)^{-1}, \tag{8}$$

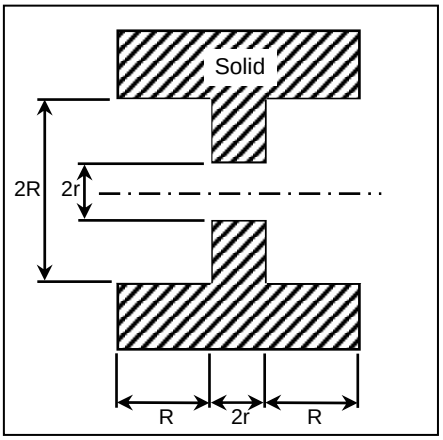

Figure 1. Geometric representation of an individual pore space channel as a constricted circular cylinder. Each channel is characterized by a pore and a throat size.

RESULTS AND DISCUSSION

The new pore structure characterization methodology was applied to a number of sandstone and carbonate samples. Typical results are shown in Fig. 2, Fig. 3 and Fig. 4 for three samples, revealing considerable differences in the apparent pore-to-throat aspect ratio. The potential usefulness of these results may be appreciated by observing that the residual mercury saturation in the Berea sample (see Fig. 5) corresponds to trapping in all pores with > 2.8. Predictions of permeability and formation factor are summarized in Table 1 and Table 2, respectively. Characteristic pore length scales for electrical

conductivity and permeability are also given in the tables. The data of Table 1 reveal that Eq. (7) yields permeability values which are, on average, a factor of 1.69 (± 0.71) different from the measured values. By comparison, Eq. (3) gives predictions that are on average a factor of 1.86 (± 0.72) different from the measured values. Thus, the new formula, Eq. (7), appears to offer no statistically significant improvement in the prediction of permeability. Formation factor values predicted by Eq. (8) (see Table 2) are, on average, a factor of 1.70 (± 0.71) different from the measured values.

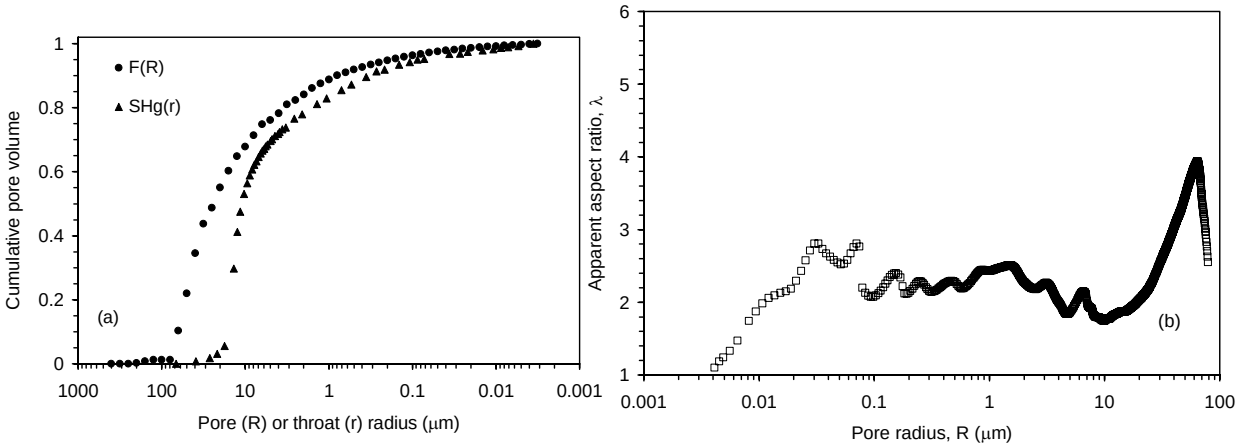

Figure 2. Distributions of pore volume by pore and access throat sizes and apparent aspect ratio for Berea sandstone sample (. = 0.202, k = 660 mD, F = 35).

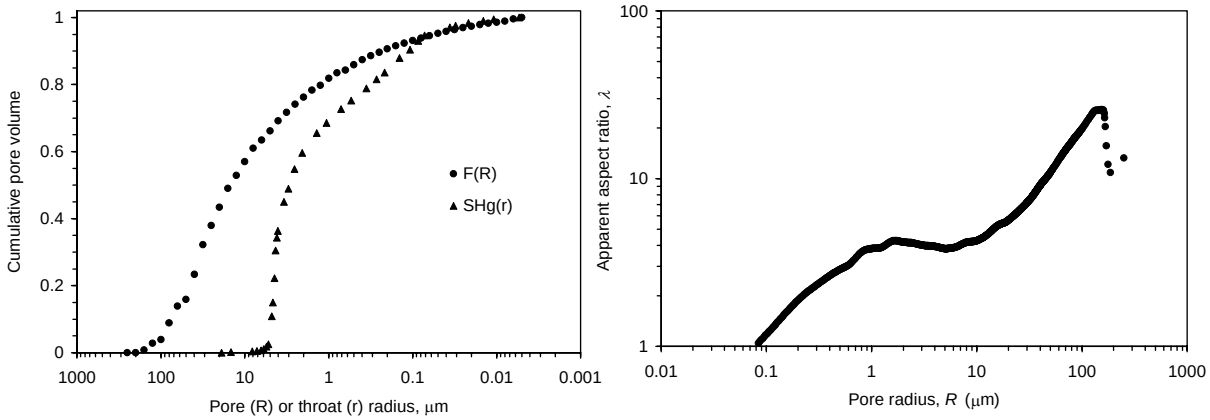

Figure 3. Distributions of pore volume by pore and access throat sizes and apparent aspect ratio for sandstone sample C6-174 (. = 0.151, k = 18.5 mD, F = 57).

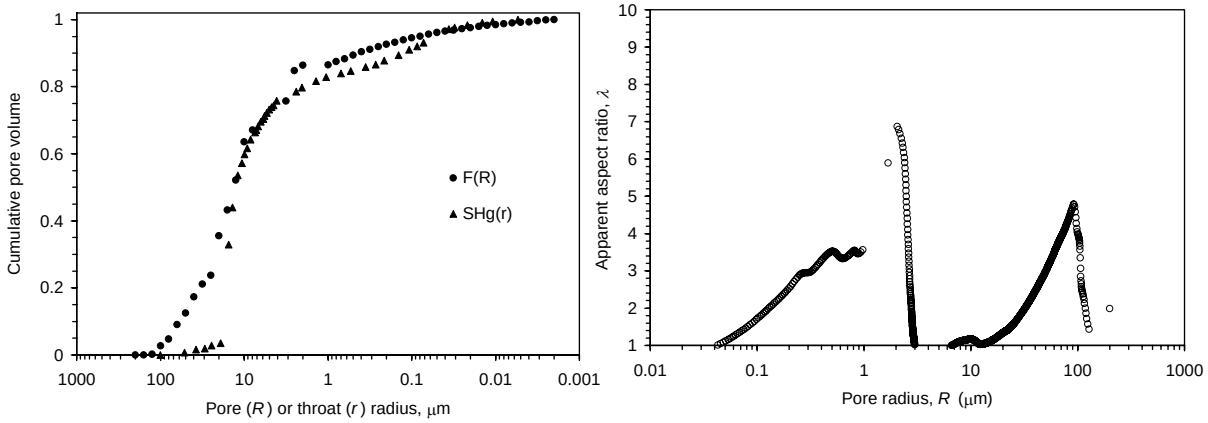

Figure 4. Distributions of pore volume by pore and access throat sizes and apparent aspect ratio for carbonate sample 13P20 (. = 0.14, k = 904 mD, F = 71).

It appears that the method proposed in this work yields pore structure information that can be used to predict both permeability and formation factor with comparable accuracy. On the contrary, Eq. (4), predicts formation factor values which are, on average, a factor of 2.80 (± 1.1) different from the measured values. We thus conclude that Eq. (8) offers a statistically significant improvement in the prediction of formation factor by CPA. This improvement is attributed to accounting for both pore *and* throat sizes in the analysis. Electrical conductivity is sensitive to a much broader spectrum of pore length scales than permeability, the latter being largely controlled by the size of largest pore throats accessible at the percolation threshold. In the model of Katz and Thompson (1987) individual pore channels are idealized as straight cylinders of uniform cross-section and their radius is identified with the radius of pore throats. Ignoring the locally convergent-divergent nature of pore channels and accounting only for the size of the constriction in the calculation of channel conductance, imparts a greater error on the electrical conductance than on the hydraulic conductance.

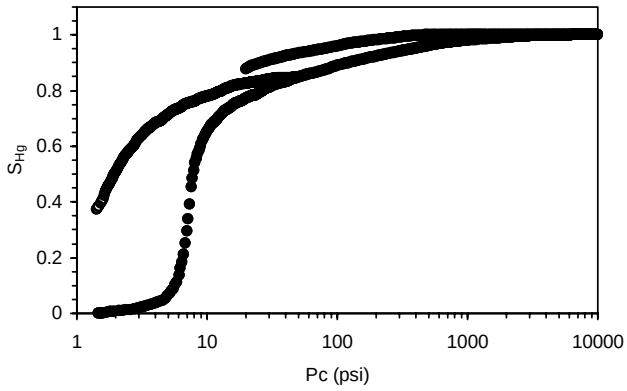

Figure 5. Mercury porosimetry data for Berea sandstone. Residual saturation (37%) corresponds to trapping of mercury in pores of aspect ratio greater than 2.8 ($R > 35$ □m).

CONCLUSIONS

Statistical fusion of BSEM and MIP data yields pore size and pore-to-throat aspect ratio information that can be used to improve predictions of permeability and formation factor by critical path analysis and may be used to assess non-wetting phase trapping.

REFERENCES

1. Amirtharaj, E.S., Ioannidis, M.A. and Macdonald, I.F., "Statistical synthesis of image analysis and mercury porosimetry for multiscale pore structure characterization", Proceedings of the Annual Symposium of the Society of Core Analysts, Pau, 2003.
2. Radlinski, A.P., Ioannidis, M.A., Hinde, A.L., Hainbuchner, M., Baron, M., Rausch, H. and Kline, S.R., "Angstrom-to-millimeter characterization of reservoir rock microstructure", *Journal of Colloid and Interface Sci.*, (2004) 274, 607-612.
3. Ehrburger-Dolle, F., Lavanchy, A. and Stoeckli, F., "Determination of the surface fractal dimension of activated carbons by mercury porosimetry", *Journal of Colloid and Interface Sci.*, (1994) 166, 451-461
4. Katz, A.J. and Thompson, A.H., "Prediction of rock electrical conductivity from mercury injection measurements", *Journal of Geophysical Research – Solid Earth and Planets*, (1987) 92(B1), 599-607.

Table 1. Prediction of permeability by Eq. (7) (k_{new}) and Eq. (3) (k_{KT}).

Sample	Lithology	k_{core} (mD)	k_{new} (mD)	$R^h_{\max}$ (□m)	$\lambda^h_{\max}$	k_{KT} (mD)	$\ell^h_{\max}$ (□m)
Berea	Sandstone	660	463	34.3	2.7	337	24.9
M4	Sandstone	450	516	45.5	2.9	413	31.4
C4-207	Sandstone	6.40	10.6	6.5	2.7	9.0	4.6
C4-137	Sandstone	12.1	4.2	15.4	6.0	8.2	5.2
C6-174	Sandstone	18.5	11.2	29.3	7.0	27.2	8.3
16Ap4	Carbonate	31.0	17.9	68.4	9.9	41.6	13.8
16Ap5	Carbonate	45.0	45.0	46.8	5.4	91.0	17.4
16Bp7	Carbonate	55.0	54.9	59.0	5.5	110.0	21.4
16Bp11	Carbonate	1.70	0.82	1.9	3.1	0.53	1.2
16Bp17	Carbonate	1200	1214	190.2	4.0	1350	94.6
16Bp18	Carbonate	250	773	40.8	2.4	480.5	33.8
16Bp19	Carbonate	20.0	24.2	49.3	5.8	47.0	17.1
13P11	Carbonate	2.30	0.88	59.2	13.3	2.87	8.9
13P20	Carbonate	904	728	17.3	1.2	264.5	27.4

Table 2. Prediction of formation factor by Eq. (8) (F_{new}) and Eq. (4) (F_{KT}).

Sample	F_{core}	F_{new}	$R^e_{\max}$ (□m)	$\lambda^e_{\max}$	F_{KT}	$\ell^e_{\max}$ (□m)
Berea	35	26.2	23.3	2.2	18.0	20.3
M4	-	42.3	35.2	2.7	23.8	26.3
C4-207	58	73.8	6.8	2.8	23.0	3.8
C4-137	39	69.0	7.4	3.6	29.8	3.8
C6-174	57	95.3	18.8	5.5	24.8	6.8
16Ap4	188	186.2	49.4	8.5	46.6	10.5
16Ap5	131	119.1	32.5	4.5	33.1	14.2
16Bp7	162	99.0	32.1	3.7	35.3	16.5
16Bp11	102	41.9	1.5	2.7	27.3	1.0
16Bp17	161	97.0	115.5	4.2	53.2	58.8
16Bp18	55	34.0	31.4	2.0	23.2	29.0
16Bp19	189	205.5	32.0	4.4	64.5	14.4
13P11	184	337.4	15.5	10.9	170.2	2.8
13P20	71	19.3	11.2	1.1	27.6	23.2